Journal of Quantitative Spectroscopy & Radiative Transfer 227 (2019) 145–151

Contents lists available at ScienceDirect

Journal of Quantitative Spectroscopy & Radiative Transfer

journal homepage: www.elsevier.com/locate/jqsrt

High-pressure and high-temperature gas cell for absorption spectroscopy studies at wavelengths up to 8 μm

Kevin K. Schwarm[a,*], Huy Q. Dinh[a], Christopher S. Goldenstein[b], Daniel I. Pineda[a], R. Mitchell Spearrin[a]

[a] Department of Mechanical and Aerospace Engineering, University of California Los Angeles, Los Angeles, CA 90095, USA
[b] School of Mechanical Engineering, Purdue University, West Lafayette, IN 47907, USA

ARTICLE INFO

Article history:
Received 17 August 2018
Revised 29 November 2018
Accepted 20 January 2019
Available online 7 February 2019

Keywords:
Optical gas cell
Absorption spectroscopy
High-temperature
High-pressure
Mid-wave infrared

ABSTRACT

An optically accessible gas cell has been designed, manufactured, and tested for the purpose of enabling spectroscopic measurements in the mid-wave infrared at both high pressures and high temperatures. The water-cooled inconel cell has been tested to sustain pressures over 200 atm or operating temperatures above 1200 K. Interchangeable sapphire or calcium-fluoride rods, transmissive up to 8 μm in wavelength, are used to span the thermal gradients at the edge of the heating zone, providing for a low-temperature seal on one end and access to a thermally uniform test section on the other. In this paper, we detail the cell design and validation testing, while highlighting cell capabilities with laser absorption measurements of gas spectra in the 2–8 μm domain at high-pressure (> 100 atm) and high-temperature (> 1200 K) conditions. The maximum cell pressure and temperature reached simultaneously was 102 atm and 1030 K. Non-ideal spectroscopic phenomena (e.g. line mixing) are revealed at the extreme conditions investigated.

1. Introduction

Many fields utilize spectroscopy for measuring gas properties. The quantitative value of spectroscopic measurements, and gas properties inferred from them, depends on the accuracy of underlying spectroscopic parameters (e.g. line intensities, line-shape characteristics) and their dependence on thermodynamic state (i.e. temperature, pressure) [1]. Thermodynamically-controlled, optically-accessible gas cells provide a stable environment for experimental determination of such spectroscopic properties.

In the field of combustion, absorption spectroscopy is a valuable tool for studying high-temperature gas dynamics, enabling in-situ species-specific measurements of gas properties [2]. Developing quantitative absorption-based sensors for combustion applications requires a detailed understanding of the fundamental spectroscopic parameters of relevant species at high temperatures and high pressures reflective of practical combustion systems. Optically-accessible gas cells capable of sustaining simultaneous high-pressure and high-temperature conditions are important for studying the spectroscopic characteristics of these species.

In recent years, multiple gas cell designs have been demonstrated to allow spectroscopic studies at elevated temperatures and/or pressures [3–7], commonly employing ceramic materials and sapphire in their construction [5,6]. The high melting point of ceramics and strength and thermal shock resistance of sapphire are ideal for high-temperature environments (> 1000 K). Gas cells built using ceramic construction with sapphire windows have been used to obtain spectroscopic measurements at temperatures up to 1700 K [6]. Few designs have been shown to simultaneously withstand high pressures (> 50 atm). Notably, Christiansen et al. recently demonstrated the first recorded spectroscopic measurements of CO_2 at > 1000 K and > 100 atm using a cell designed with sapphire windows bonded to ceramic tubes [5]. These designs enable novel spectroscopic studies of numerous near-infrared (and some mid-infrared) molecular absorption bands.

However, for many combustion-relevant species, fundamental vibrational frequencies lie in the mid-infrared region beyond the transmission window of sapphire. The high absorption strength of these fundamental bands is important in enabling sensitive measurements in applications with short optical pathlengths or small molecular concentrations [2]. Sapphire optical windows—which exhibit exceptional transmission in the near-wave infrared—become opaque in the mid-wave infrared (~ 5 μm). Moreover, elevated temperatures shift the sapphire transmission cut-off toward shorter wavelengths [11]. As a result, gas cell designs with sapphire windows do not facilitate spectroscopic investigations of many fundamental absorption bands of interest, especially at high-

* Corresponding author.
E-mail address: kschwarm@g.ucla.edu (K.K. Schwarm).

https://doi.org/10.1016/j.jqsrt.2019.01.029
0022-4073/

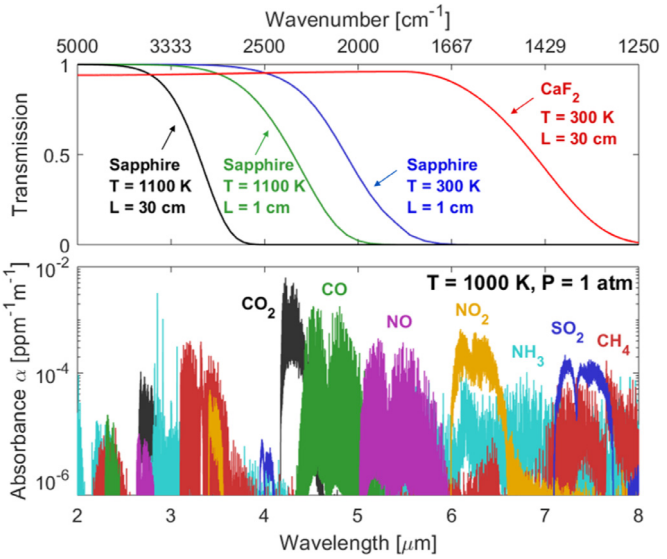

Fig. 1. Transmission of light through sapphire [8] and calcium fluoride [9] (top) compared to absorption spectra of species relevant to combustion [10] (bottom).

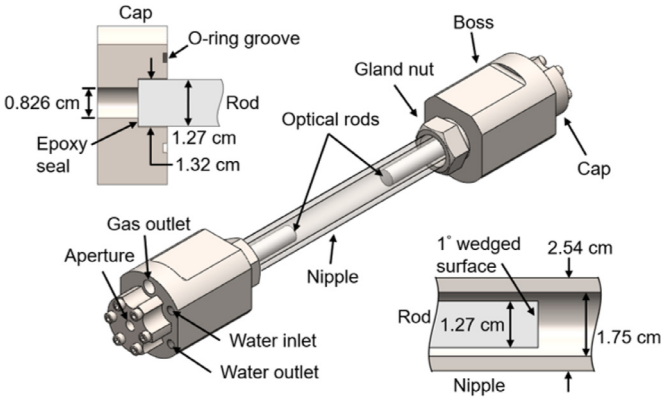

Stress analysis at test conditions: T = 1000 K, P = 200 atm

Component	Stress (MPa)	Factor of Safety
Nipple	65.0	4.24
CaF_2 rods	21.2	6.77
Cap	45.4	5.84
Cap bolts	98.0	4.93

Inconel 625 strength vs. temperature

Temperature (K)	Yield Strength (MPa)
296	496
1000	430
1100	380
1200	190

Fig. 2. Detailed view of the high-pressure, high-temperature gas cell with critical design considerations and material data [15,16].

temperature conditions typical of combustion systems. This limitation is displayed in Fig. 1, where the strong absorption bands of key species (e.g. CO, NO, NO_2) are inaccessible in part or whole to existing gas cell designs with sapphire windows.

Unfortunately, optical materials that transmit beyond the transmission range of sapphire are generally less robust and require particular concern at elevated temperature. In this work, we present a gas cell that utilizes calcium fluoride (CaF_2) rods. Although using CaF_2 presents its own challenges (which are addressed in this paper), the material transmits light up to 8 μm in wavelength and thus enables measurements of numerous strong fundamental absorption bands (even at high temperatures) not accessible with existing cell designs. The present gas cell also uses Inconel 625 rather than a ceramic material for the non-optical cell components within the heating zone. This alloy exhibits higher strength at high temperatures than other commonly used metals and is more ductile and elastic than ceramics, thus fatiguing at lower rates [12]. This paper discusses the design of this high-temperature, high-pressure gas cell and the unique technical aspects involved with its construction and operation. The cell is validated for use in spectroscopic measurements by evaluating the temperature uniformity over a range of test conditions and comparing measurement results of well-known spectra to simulations using the current HITEMP [13] and HITRAN [14] databases. The experimental setup is then demonstrated to measure the absorption spectra of CO and CH_4 in the mid-wave infrared at conditions not previously explored, highlighting the unique capabilities of the cell and revealing spectroscopic features not previously observed.

2. Gas cell and experiment design

The mechanical design and material selection of the gas cell enable operation at high temperatures (> 1200 K), high pressures (> 200 atm), and transmission up to 8 μm. Due to compromises in material properties at elevated temperature, these design targets are more difficult to achieve simultaneously. An important objective in the cell design was thus to achieve simultaneous operation at > 1000 K in temperature and > 100 atm in pressure while accessing the wavelength domain from 0.3 to 7.5 μm. Fig. 2 shows physical details of the gas cell along with relevant mechanical design calculations. The cell body is made from Inconel 625 alloy, chosen for its machinability, ductility, high corrosion resistance, and high thermal conductivity that promotes a uniform temperature over the test region. Additionally, Inconel 625 exhibits high strength and maintains this strength at elevated temperatures, unlike other commonly used metals [15]. Coned and threaded metal-to-metal seals are used (High Pressure Equipment Co.) with the exception of the cap, which uses an O-ring seal.

A critical design consideration in the gas cell is sealing the optical component to the metal body, while accessing the thermally-uniform, high-temperature test section. The optical components used in this gas cell are interchangeable CaF_2 or sapphire rods 15.0 cm in length, which allow for a low-temperature seal outside of the heating zone, while spanning the thermal gradient of the furnace to access the test section. A 1° wedged surface at one end of each rod reduces constructive and destructive optical interference. CaF_2 is chosen because of its ability to transmit light at wavelengths up to 8 μm. However, CaF_2 is less robust than sapphire [16], especially at elevated temperatures, having lower strength, higher sensitivity to thermal shock, and susceptibility to degrading reaction with water vapor [17]. Sensitivity to thermal shock is associated with relatively high thermal expansion and low thermal conductivity. Clearance around the rod within the cap allows thermal expansion without creating additional stresses. The design of the boss component includes water cooling channels that maintain the caps at low enough temperatures such that they can be sealed by silicon O-rings rated to 478 K. A high-temperature epoxy (EPO-TEK T7109), limited to sustained operation below 573 K, bonds the interchangeable optical rods to the caps and also seals the gas cell. These sealing surfaces lie outside of the heating zone of the furnace and the water cooling prevents failure of these seals, even when the furnace temperature exceeds 1200 K.

Since the rods are bonded only to the caps—which are removable—the gas cell can be easily modified for different applications. When transmittance in longer wavelengths is not required, the CaF_2 rods can be replaced with sapphire rods for increased durability. Additionally, rods of different lengths can be installed for pathlength modification as may be appropriate for different applications.

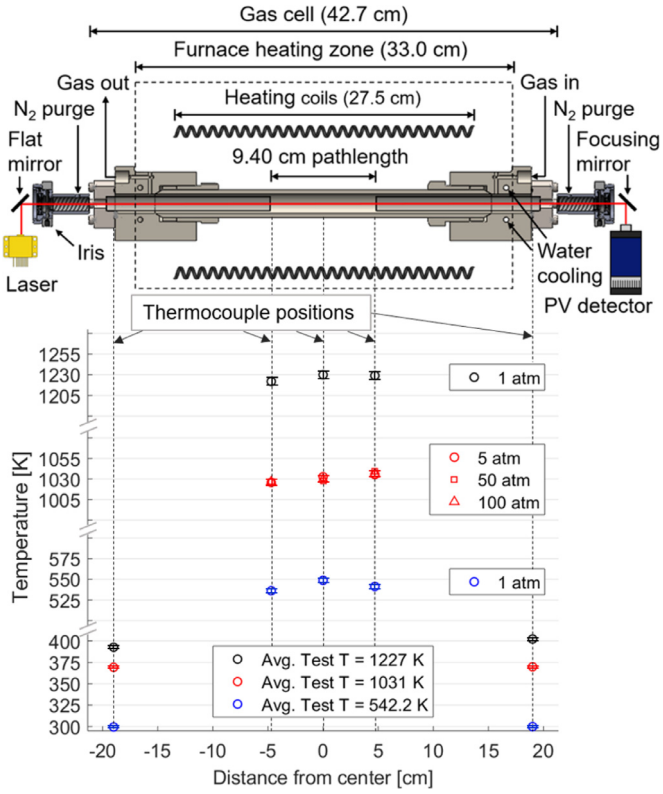

Fig. 3. Schematic of experimental setup for spectroscopic measurements through the high-P/T gas cell, displayed with measured temperatures at representative operating conditions.

The gas cell is housed inside an insulated, temperature-controlled furnace with eight heating coils, capable of maintaining an internal temperature of 1473 K. The critical dimensions are shown in Fig. 3. The heating zone comprises an internal cavity surrounded by insulation. The measurement pathlength of the gas cell is small relative to the length of the heating zone, promoting a steady, uniform temperature in the test region. Cooling channels in the cell are located near the boundary of the heating zone.

Chilled laboratory water delivered to the cooling channels at 8 gallons/h in each boss maintains the operating temperature of the caps under the limits of the O-rings and epoxy. Temperatures are monitored with multiple K-type thermocouples attached to the nipple of the gas cell and equally spaced over the test region. Their positions are shown in Fig. 3. The cap temperatures are also monitored to ensure safe operating conditions for the seals during experiments. All thermocouples used have an accuracy of 0.75% for the expected operating temperature range and these uncertainties are shown as error bars in Fig. 3. The test gas is introduced to the test cavity via channels in the boss as shown in Fig. 3, and delivered to the gas cell through stainless steel tubing connected to a gas manifold. Pressure transducers connected to this manifold provide measurements of the pressure inside the gas cell. For test pressures up to 3000 psig, variable capacitance pressure transducers (Setra GCT-225) are used with an accuracy of $\pm 0.25\%$ of the full scale. For test pressures below 1000 Torr, a dual capacitance manometer (MKS Baratron 627B) is used with an accuracy of $\pm 0.12\%$.

The optical rods traverse the thermal gradient of the heating zone and form the optical pathlength (9.4 cm). This short pathlength is conducive to studying strong fundamental rovibrational transitions in the mid-infrared. The length of the rods also reduces the likelihood that the windows will crack during high pressure experiments. At elevated temperatures, changes in the optical pathlength due to thermal expansion must be considered. For example, it was determined that for sapphire rods, the pathlength increases by 2.7 $\pm$ 0.5% at 1230 K; with the uncertainty due to variation in data for the different coefficients of thermal expansion. As mentioned, CaF_2 degrades significantly in the presence of moisture above 873 K [17], and more slowly at lower temperatures, so a purge system was developed, as shown in Fig. 3, to supply a continuous flow of dry inert N_2 to the outside surface of these rods to prevent degradation of the optical surface by humid ambient air. This purge system includes irises on one end that promote the N_2 flow toward the rods while allowing optical access to the gas cell.

3. Validation testing

The sealing of the gas cell—and subsequent purity of the mixtures under investigation—is critical to the accuracy and reliability of spectroscopic measurements. Typical measurement durations span about 20–90 s, from the introduction of the test gas into the cell to the capture of the data. The effect of leak rate on the measurement must be negligible at pressures of interest. The tightness of the gas cell was evaluated under expected operating conditions (high pressures, high temperatures). Under vacuum, the leak rate was measured as 6 mTorr/min at 300 K and 38 mTorr/min at 1000 K. Under 103 atm pressure at 1000 K, the leak rate is approximately 0.3 atm/min (or 0.26%/min) with pure helium as the test gas. At the maximum design and test pressure of 204 atm and 300 K, the leak rate was approximately 0.4%/min. It should be noted that given the leak rates at these high pressures, the user must exercise caution and properly exhaust the leaked gases from the laboratory.

A known and uniform gas temperature (monitored by aforementioned thermocouples shown in Fig. 3) in the test section is also critical for accurate and reliable measurements. For a test temperature of 542 K, the uniformity over the test region reported by the thermocouples is ± 7 K; this number incorporates both the aforementioned sensor accuracy and the variation in measurement across the cell. At a test temperature of 1031 K, the temperature gradient shows no strong relationship with gas pressure, and the average temperature uniformity is ± 9 K. At a test temperature of 1227 K, the uniformity over the test region is ± 10 K. For temperatures above 600 K, the inherent uncertainty in each thermocouple ($\pm 0.75\%$) exceeds these non-uniformities. The use of thermocouple measurements on the outside of the cell to infer the gas temperature and temperature uniformity inside the cell is justified with a more detailed thermal analysis outlined in the appendix of this manuscript. At the highest temperatures, the water cooling is able to maintain an average cap temperature of 397 K, below the rated temperatures of the epoxy window seals and the cap O-rings.

4. Spectroscopic measurements

To test and further validate the gas cell capabilities, we conducted infrared laser absorption measurements of CO and CH_4 at (1) high temperatures and low pressures, (2) low temperatures and high pressures, and (3) simultaneous high temperatures and high pressures. For all measurements, a scanned-wavelength direct absorption technique was utilized with laser output line-width significantly more narrow than the measured spectral features.

Absorption of several lines of the vibrational overtone band of CO near 2.3 μm were measured with a diode laser in pure (99.5%) CO at 1227 K and 755 Torr using sapphire rods, representing an upper limit in temperature of the cell. These absorbance measurements, along with corresponding simulations made with HITEMP 2010 [13], are shown in Fig. 4. For the simulation shown, CO–CO line-broadening parameters were approximated using CO–N_2

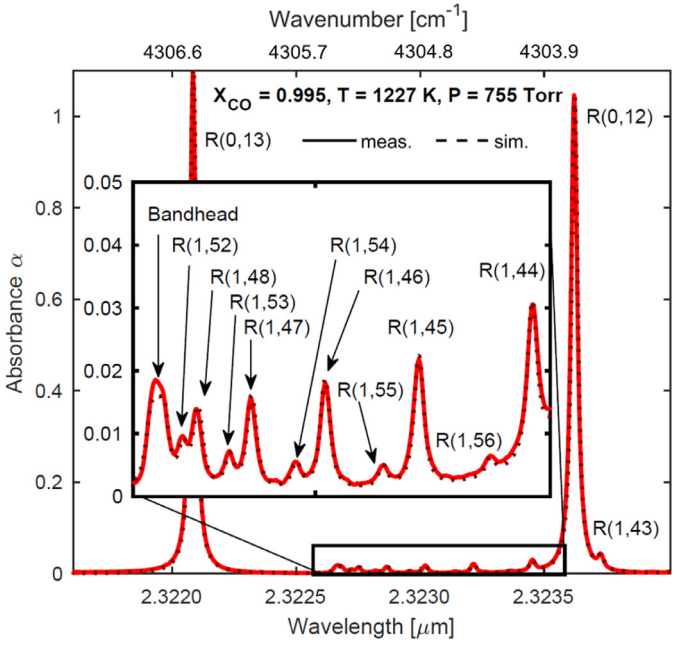

Fig. 4. Absorbance of the first overtone bandhead of CO at 1227 K with corresponding simulation based on HITEMP 2010 [13].

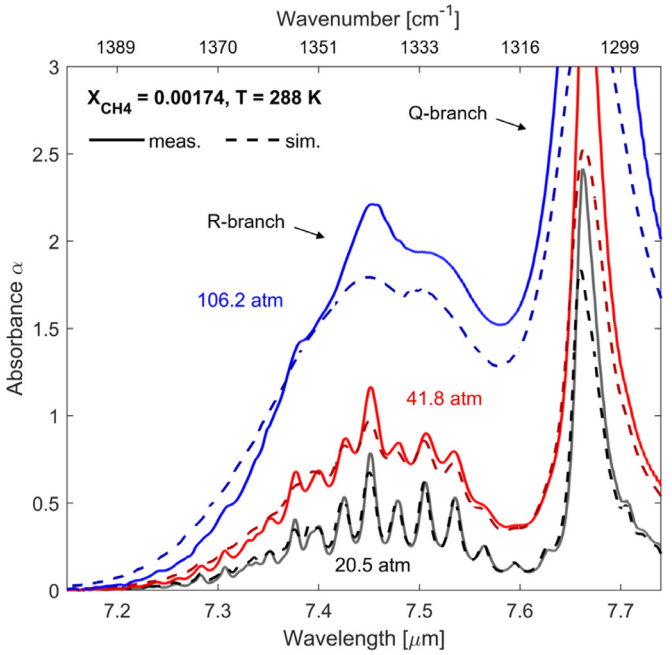

Fig. 5. Absorbance of the ν_4 band of CH_4 at 288 K and pressures up to 106 atm with corresponding simulations based on HITRAN 2016 [14].

parameters provided by Hartmann et al. [18]. The spectra shown include the well-characterized R(0,12) and R(0,13) lines, the linestrengths of which are reported with 1% uncertainty in the HITRAN database [14]. Given the pressure, path-length, and mole fraction known within 0.12%, 0.5%, and 0.1%, respectively, a direct gas temperature can be determined based on the integrated absorbance areas of these well-known lines. This inference using the isolated R(0,13) line yields a mean temperature measurement of 1217 ± 14 K, which is within the uncertainty of the thermocouple measurement of 1227 ± 10 K. Weaker but discernible spectral lines shown include R(43)–R(48) and R(52)–R(56) with minimum detectable absorbance of approximately 5e–4. Some disagreement is observed in the bandhead, which includes the R(49)–R(51) lines. Data such as these are useful for the refinement and development of improved high-temperature spectroscopic models.

To demonstrate pressure capability and wavelength range, absorption of the ν_4 band of CH_4 was measured using an EC-QCL [19,20] with a tuning range of 7–7.8 μm (1280–1427 cm^{-1}), and the results are shown in Figs. 5 and 6. The broad tuning range of the laser enabled spectral resolution of a large fraction of the absorption band. The test gas mixtures comprised small concentrations of CH_4 in an N_2 bath gas created barometrically. These measurements were compared to simulations based on the HITRAN 2016 database [14].

For the low-temperature measurements at 288 K shown in Fig. 5, the measured absorbance in the R-branch generally matches the simulation at pressures up to ~20 atm, while the simulation underpredicts the measurement in the Q-branch. This underprediction may be attributed to line mixing effects that shift absorption intensity from weak lines to strong lines and are more pronounced in crowded spectra [21]. This trend increases in magnitude and is seen in the R-branch as well as the test pressure is increased. At high pressures, line mixing is evident at all test temperatures, as seen in the left of Fig. 6. The measured peak absorbance near 7.66 μm (1305 cm^{-1}) and 7.46 μm (1340 cm^{-1}) is consistently greater than that predicted by simulation, while for the weaker portions of the band at wavelengths lower than around 7.46 μm (1350 cm^{-1}), the measurement is lower than predicted. Pieroni et al. [22] and Tran et al. [23] observed similar trends in the ν_3 and ν_4 bands of CH_4, supporting the line mixing observations noted here.

To demonstrate and validate the simultaneous high-temperature and high-pressure capability of the cell, absorption of the P(0,31) line of the fundamental vibrational band of CO was measured in a mixture of 0.4% CO in 99.6% N_2 at 1031 K and various pressures up to 102.4 atm. This well-characterized CO line has been previously used for measurements in high-pressure combustion environments [24] owing to its relatively high linestrength and isolation from neighboring lines, and thus may be considered a more reliable validation benchmark. The measurement range covers 4.978–4.980 μm (2008–2009 cm^{-1}), which is limited by the scanning range of the DFB-QCL. Absorption measurements are displayed alongside simulations based on the HITEMP 2010 database in Fig. 6. Generally, the gas cell measurements show good agreement with simulation. It should be noted that at very high pressures, the background signal used to yield absorbance was observed to attenuate independent of absorption (possibly due to refraction through the dense gas). To account for this effect, the gas cell would be filled with a non-absorbing bath gas (in this case N_2) to the target pressure to reproduce this effect and collect a reliable background signal [25].

The absorbance of the R-branch of CH_4 at 60 atm and various temperatures is shown in the left of Fig. 6. The plots show a clear relationship between increasing gas temperature and the increasing underestimation of molecular absorption in the R branch of the ν_4 band of CH_4 by the simulation. This trend is not fully explained by line mixing alone, as increased temperature reduces gas density. Rather, this disagreement suggests the existence of high lower-state energy lines not listed in the current HITRAN database which are only active at higher temperatures. This suggestion is supported by the recent work of Ghysels et al. [7], who performed measurements of the $2\nu_3$ band of CH_4 near 1000 K. They found significant differences between measured absorption features and those predicted by simulations at high temperatures, attributed in part to missing lines active at elevated temperature.

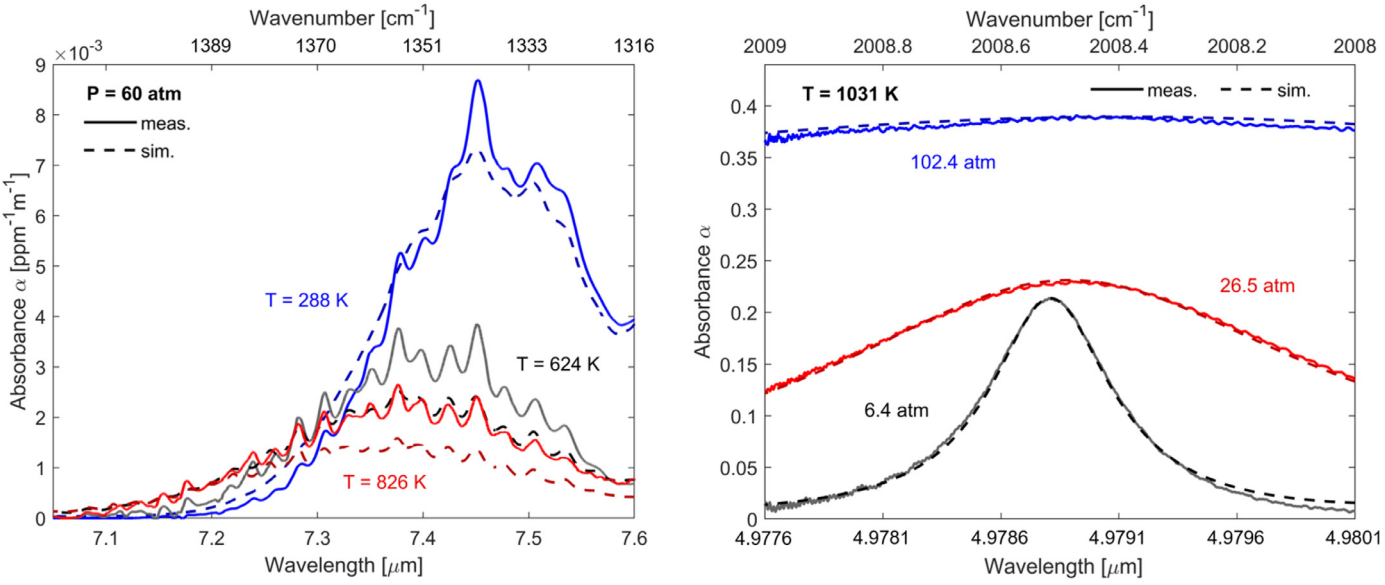

Fig. 6. Simultaneous high-temperature and high-pressure measurements of the R branch of the ν_4 band of CH_4 (left) and the P(0,31) transition of CO (right) with corresponding simulations based on HITRAN 2016 (CH_4) [14] and HITEMP 2010 (CO) [13].

5. Conclusions

An optically-accessible gas cell design presented in this paper demonstrates a capability of sustaining simultaneous high-pressure and high-temperature conditions for well-controlled spectroscopy studies. When access to the mid-wave infrared is needed, the use of CaF_2 optical rods facilitates spectroscopic measurements up to 8 μm. This extends the accessible wavelength range beyond that provided by sapphire optics by approximately 3 μm, enabling studies of the fundamental vibrational absorption bands of several species critical to combustion processes. The use of this gas cell for sensitive spectroscopic measurements was validated with an evaluation of leak-tightness and temperature uniformity over the test region for a wide range of pressures and temperatures, along with satisfactory measurement of a well-understood fundamental transition of CO at high temperatures and high pressures. A maximum test pressure of 204 atm and test temperature of 1227 K highlight the range of the cell when focusing on one state variable, while simultaneous high-temperature (1031 K) and high-pressure (102.4 atm) measurements using the CaF_2 rods were also demonstrated.

The utility of this gas cell design to investigate non-ideal spectroscopic phenomena at extreme conditions was proven by example measurements. Namely, novel measurements of the ν_4 band of CH_4 at various high-temperature and high-pressure conditions were made, showing evidence of line mixing effects and missing lines not accounted for in current spectroscopic databases. Future studies using this unique cell design will directly inform the improvement of spectroscopic models at conditions relevant to combustion and other high-temperature environments where quantitative sensing depends on the accuracy of the underlying spectroscopic properties.

Acknowledgments

The work presented in this paper was supported by the U.S. National Science Foundation, Award No. 1752516. The authors acknowledge the experimental assistance of Daniel D. Lee, Fabio A. Bendana, and Chuyu Wei. A special thanks to J. Kriesel and Opto-Knowledge Systems, Inc. for providing the EC-QCL.

Appendix A

In this appendix we briefly outline a one-dimensional finite difference heat transfer model used to justify the assumptions that (1) the thermocouple measurements on the cell wall are sufficient to describe the gas temperature within reported uncertainty and (2) that the temperature in the gas test section is uniform within the range reported. For brevity, we skip the derivation of the finite-difference forms of the governing equations, but these are readily available in the literature [26,27]. At the end of the appendix, we compare this 1-D model to a 3-D heat transfer simulation (using the same boundary conditions and heat transfer modes) using commercial software (ANSYS Mechanical APDL) on a single test case for independent verification of the thermal analysis.

A.1. Model assumptions and setup

A diagram of the computational domain depicting a symmetric half of the gas cell is shown in Fig. 7. The domain comprises the inconel cell wall, one of the sapphire rods, and a gas in the cell. Recorded thermocouple measurements on the outside of the cell wall are shown as T_c, T_1, and T_2. For some calculations we divide the computational domain into two sections, the rod section (Domain 1), and the gas test section (Domain 2).

Insets in Fig. 7 show the considered methods of heat transfer from the center of the cell to the ends of the cell. The following assumptions are made:

- The thermal resistance along the inconel wall is much less than that between the wall and the gas.
- The gas has the thermal properties of air.
- The heat transfer in the sapphire rod and the inconel cell wall in Domain 1 are dominated by one-dimensional conduction axially, while natural convection and radiation dominate radially.
- For natural convection, gas temperature $T_g(x)$ in Domain 1 is assumed to be the average of the inconel wall temperature $T_w(x)$ and the rod temperature $T_r(x)$ at the same position x.
- For the gas in Domain 2, conduction between the cell wall and the gas dominates radially, while gas–gas conduction dominates axially.

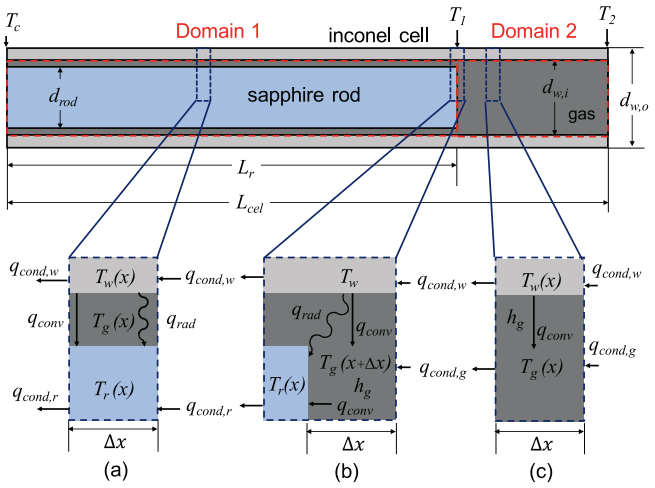

Fig. 7. Gas cell domains for 1-D finite-difference heat transfer calculation, with energy balance diagrams for the heat transfer considered in different regions of the cell.

A.2. Governing equations

A simplified finite-difference expression of the 1-D heat conduction equation [26] for the temperature at position x in the inconel wall, $T_w(x)$ (Fig. 7(a)–(c)), utilizing the Crank–Nicolson method [27], is:

$$T_w(x) = \frac{\alpha_i(x+\Delta x)\Delta t}{\Delta x^2}T_w(x+\Delta x) + \left(1 - 2\frac{\alpha_i(x)\Delta t}{\Delta x^2}\right)T_w(x) + \frac{\alpha_i(x-\Delta x)\Delta t}{\Delta x^2}T_w(x-\Delta x) \quad (1)$$

$\alpha_i(x)$ is the thermal diffusivity of inconel at position x, which changes throughout the domain due to the temperature dependence of thermal conductivity $k_i(x)$ and specific heat capacity $c_{p,i}(x)$, while the density of inconel ρ_i is assumed to be constant. The finite-difference expression for the temperature of the optical rod is similar, but includes terms for heat transfer via natural convection and thermal radiation, as indicated in Fig. 7(a) [26]:

$$T_r(x) = \frac{\alpha_s(x+\Delta x)\Delta t}{\Delta x^2}T_r(x+\Delta x) + \left(1 - 2\frac{\alpha_s(x)\Delta t}{\Delta x^2}\right)T_r(x) + \frac{\alpha_s(x-\Delta x)\Delta t}{\Delta x^2}T_r(x-\Delta x) + h_{\text{nat}}(x)\left(\frac{A_{s,r}/A_{c,r}}{\rho_s c_{p,s}(x)}\frac{\Delta t}{\Delta x}\right)(T_w(x) - T_r(x)) + h_{\text{rad}}(x)\left(\frac{A_{s,w}/A_{c,r}}{\rho_s c_{p,s}(x)}\frac{\Delta t}{\Delta x}\right)(T_w(x) - T_r(x)) \quad (2)$$

In Eq. (2), $A_{s,r}$ is the surface area of the sapphire rod for a finite length Δx, $A_{s,w}$ is the corresponding inner surface area of the inconel cell wall, and $A_{c,r}$ is the cross-sectional area of the optical rod. The heat transfer coefficient $h_{\text{nat}}(x)$ due to natural convection between two concentric cylinders and associated expressions are available in Bergman et al. [26]. The effective radiation heat transfer coefficient $h_{\text{rad}}(x)$ [26] is used for computational convenience, in which the view factor for two concentric cylinders [26] is assumed. Our model assumes constant emissivities $\epsilon_i = 0.55$ [28] and $\epsilon_s = 0.55$ [26] based on available literature values for similar inconel alloys and aluminum oxide, respectively. At the boundary of Domain 2, shown in Fig. 7(b), where $x = L_r$, the terms:

$$\frac{h_g}{\rho_s c_{p,s}}\frac{\Delta t}{\Delta x}(T_{g,\text{avg}} - T_r(L_r)) + \frac{h_{\text{rad},f}}{\rho_s c_{p,s}}\frac{\Delta t}{\Delta x}(T_{w,\text{avg}} - T_r(L_r)) \quad (3)$$

are included in Eq. (2) to account for axial heat transfer due to convection and radiation at the face of the optical rod from the gas and the inconel cell walls, respectively. h_g is assumed to be 25 W/m^2, and $T_{g,\text{avg}}$ is the average temperature of the gas between the rods. $T_{w,\text{avg}}$ is the average temperature of the inconel cell wall in Domain 2 and $h_{\text{rad},f}$ is the effective radiation heat transfer coefficient, using a view factor for the inside surface of a right circular cylinder to one of its circular faces [28]. In Domain 2, shown in Fig. 7(c), the heat transfer in the gas is modeled similarly to that of the inconel wall and optical rod:

$$T_g(x) = \frac{\alpha_g(x+\Delta x)\Delta t}{\Delta x^2}T_g(x+\Delta x) + \left(1 - 2\frac{\alpha_g(x)\Delta t}{\Delta x^2}\right)T_g(x) + \frac{\alpha_g(x-\Delta x)\Delta t}{\Delta x^2}T_g(x-\Delta x) + h_g\left(\frac{A_{s,w}/A_{c,w}}{\rho_g(x)c_{p,g}(x)}\frac{\Delta t}{\Delta x}\right)(T_w(x) - T_g(x)) \quad (4)$$

A major difference for Eq. (4) is that $\rho_g(x)$ is not constant, but determined by an equation of state for the gas cell test pressure and $T_g(x)$.

A.3. Boundary conditions

The boundary conditions of Domains 1 and 2 constrain the system model and are detailed here. The cell is axially symmetric and there is a symmetric adiabat in the plane $x = L_{\text{cel}}$. This is accomplished numerically with ghost points beyond the domain boundary [27]. $T_w(x)$ has fixed temperatures near each end of each domain. For Domain 2, in the middle of the cell (the right of Fig. 7), the temperatures at the outside surface of the inconel cell wall are specified by T_1 and T_2. Likewise, Domain 1 is bounded by T_1 and T_c. $T_w(x)$ is modeled independently of the inside of the cell since T_1, T_2, and T_c are known and the heat transfer in the cell wall is dominated by conduction. $T_w(x)$ is fixed once it is determined, and these temperatures bound the system. Additionally, all points at $x = 0$ are at T_c.

A.4. Numerical solution

Although the model is transient, we solve for the temperature profile of the inconel cell separately from those of the optical rod and the gas, since we are primarily concerned with the steady state condition. We first solve for $T_w(x)$ using Eq. (1), initially assuming linear temperature profiles spanning $T_w(0) = T_{\text{cap}}$ to $T_w(L_r) = T_1$ for Domain 1 and $T_w(L_r) = T_1$ to $T_w(L_{\text{cel}}) = T_2$ for Domain 2. The domains for $T_w(x)$ are solved as a single domain. A timestep Δt and grid cell size Δx are chosen to ensure numerical stability while also keeping computational cost reasonable [27], and the model is run for enough timesteps to converge on a final profile for $T_w(x)$.

Once $T_w(x)$ is known and fixed, we solve for $T_r(x)$ and $T_g(x)$ simultaneously using Eqs. (2) and (4). For the optical rod, we estimate an initial linear temperature profile spanning $T_r(0) = T_c$ to $T_r(L_r) = 0.5T_1$ for Domain 1. For the gas, $T_g(x) = (T_w(x) + T_r(x))/2$

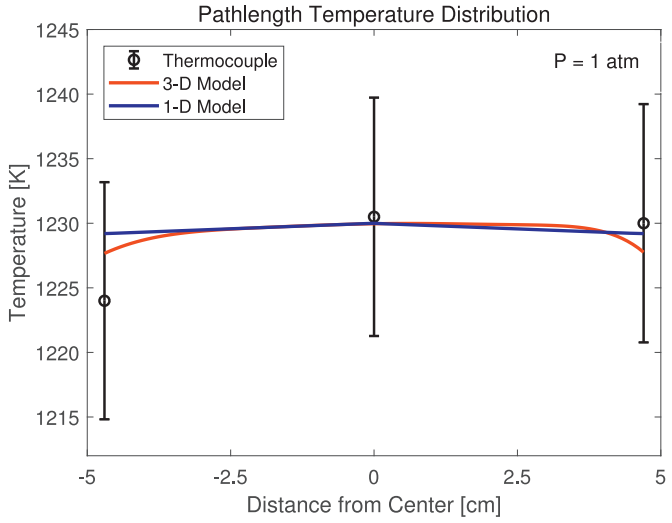

Fig. 8. Results for 1-D finite-difference heat transfer model and 3-D heat transfer model alongside thermocouple measurements for the test shown in Fig. 4.

in Domain 1, while a uniform profile is initially assumed for Domain 2, with $T_g(x > L_r) = (T_w(L_r) + T_r(L_r))/2$. We determine appropriate Δt and Δx, and allow the model to run to convergence.

A.5. Test case

To justify the assumptions regarding the gas temperature measurement and the test section temperature uniformity, we employ the model to analyze the test conditions shown in Fig. 4. The thermocouple measurements from the experiment are used as inputs for T_c, T_1, and T_2, and the results for the gas temperature distribution are shown in Fig. 8. For the 3-D model, asymmetries reported by the thermocouple measurements were included, while complete symmetry was assumed for the 1-D model. It is shown that the predicted gas temperature distribution for both models falls entirely within the thermocouple experimental uncertainty and reported temperature uniformity range. Importantly, the symmetric 1-D model predicts temperatures within 0.3% of those of the 3-D model (which accounts for finite wall and rod thicknesses), providing additional confidence in the assumptions of the measurements in the cell. Thus, the assumptions that the thermocouples can be used to infer the gas temperature distribution and uniformity are justified for the most extreme temperature conditions discussed in this manuscript.

References

[1] Hanson RK, Spearrin RM, Goldenstein CS. Spectroscopy and optical diagnostics for gases. Springer; 2016. doi:10.1007/978-3-319-23252-2.
[2] Goldenstein CS, Spearrin RM, Jeffries JB, Hanson RK. Infrared laser-absorption sensing for combustion gases. Prog Energy Combust Sci 2017;60:132–76. doi:10.1016/j.pecs.2016.12.002.
[3] Rieker GB, Liu X, Li H, Jeffries JB, Hanson RK. Measurements of near-IR water vapor absorption at high pressure and temperature. Appl Phys B Lasers Opt 2007;87(1):169–78. doi:10.1007/s00340-006-2523-4.
[4] Spearrin RM, Schultz IA, Jeffries JB, Hanson RK. Laser absorption of nitric oxide for thermometry in high-enthalpy air. Meas Sci Technol 2014;25(12). doi:10.1088/0957-0233/25/12/125103.
[5] Christiansen C, Stolberg-Rohr T, Fateev A, Clausen S. High temperature and high pressure gas cell for quantitative spectroscopic measurements. J Quant Spectrosc Radiat Transfer 2016;169:96–103. doi:10.1016/j.jqsrt.2015.10.006.
[6] Melin ST, Sanders ST. Gas cell based on optical contacting for fundamental spectroscopy studies with initial reference absorption spectrum of H_2O vapor at 1723 K and 0.0235 bar. J Quant Spectrosc Radiat Transfer 2016;180:184–91. doi:10.1016/j.jqsrt.2016.04.009.
[7] Ghysels M, Vasilchenko S, Mondelain D, Béguier S, Kassi S, Campargue A. Laser absorption spectroscopy of methane at 1000 K near 1.7 μm: a validation test of the spectroscopic databases. J Quant Spectrosc Radiat Transfer 2018;215:59–70. doi:10.1016/j.jqsrt.2018.04.032.
[8] Thomas ME, Joseph R, Tropf WJ. Infrared transmission properties of sapphire, spinel, yttria, and ALON as a function of temperature and frequency. Appl Opt 1988;27(2):239–45.
[9] The Crystran handbook of infra-red and ultra-violet optical materials. 3rd ed. Poole, UK: Crystran Ltd; 2016.
[10] Goldenstein CS, Miller VA, Spearrin RM, Strand CL. SpectraPlot.com: integrated spectroscopic modeling of atomic and molecular gases. J Quant Spectrosc Radiat Transfer 2017;200:249–57. doi:10.1016/j.jqsrt.2017.06.007.
[11] Oppenheim UP, Even U. Infrared properties of sapphire at elevated temperatures. J Opt Soc Am 1962;52(9):1078_1. doi:10.1364/JOSA.52.1078_1.
[12] Ritchie R. Fatigue of brittle materials. In: Comprehensive structural integrity. Elsevier; 2003. p. 359–88. doi:10.1016/B0-08-043749-4/04025-8.
[13] Rothman LS, Gordon IE, Barber RJ, Dothe H, Gamache RR, Goldman A, Perevalov VI, Tashkun SA, Tennyson J. HITEMP, the high-temperature molecular spectroscopic database. J Quant Spectrosc Radiat Transfer 2010;111(15):2139–50. doi:10.1016/j.jqsrt.2010.05.001.
[14] Gordon IE, Rothman LS, Hill C, Kochanov RV, Tan Y, Bernath PF, Birk M, Boudon V, Campargue A, Chance KV, Drouin BJ, Flaud JM, Gamache RR, Hodges JT, Jacquemart D, Perevalov VI, Perrin A, Shine KP, Smith MA, Tennyson J, Toon GC, Tran H, Tyuterev VG, Barbe A, Császár AG, Devi VM, Furtenbacher T, Harrison JJ, Hartmann JM, Jolly A, Johnson TJ, Karman T, Kleiner I, Kyuberis AA, Loos J, Lyulin OM, Massie ST, Mikhailenko SN, Moazzen-Ahmadi N, Müller HS, Naumenko OV, Nikitin AV, Polyansky OL, Rey M, Rotger M, Sharpe SW, Sung K, Starikova E, Tashkun SA, Auwera JV, Wagner G, Wilzewski J, Wcisło P, Yu S, Zak EJ. The HITRAN2016 molecular spectroscopic database. J Quant Spectrosc Radiat Transfer 2017;203:3–69. doi:10.1016/j.jqsrt.2017.06.038.
[15] Special Metals Corporation. Inconel alloy 625. Technical Report; 2013.
[16] Harris DC. Durable 3–5 μm transmitting infrared window materials. Infrared Phys Technol 1998;39(4):185–201. doi:10.1016/S1350-4495(98)00006-1.
[17] Ropp R. Group 17 (H, F, Cl, Br, I) alkaline earth compounds. In: Encyclopedia of the alkaline earth compounds, vol. 17. Elsevier; 2013. p. 25–104. doi:10.1016/B978-0-444-59550-8.00002-8.
[18] Hartmann JM, Rosenmann L, Perrin MY, Taine J. Accurate calculated tabulations of CO line broadening by H_2O, N_2, O_2, and CO_2 in the 200–3000 K temperature range. Appl Opt 1988;27(15):3063. doi:10.1364/AO.27.003063.
[19] Phillips MC, Taubman MS, Kriesel J. Use of external cavity quantum cascade laser compliance voltage in real-time trace gas sensing of multiple chemicals. In: Razeghi M, Tournié E, Brown GJ, editors. Proceedings of SPIE - the international society for optical engineering; 2015. p. 93700Z. doi:10.1117/12.2080852.
[20] Kriesel JM, Makarem CN, Phillips MC, Moran JJ, Coleman ML, Christensen LE, Kelly JF. Versatile, ultra-low sample volume gas analyzer using a rapid, broad-tuning ECQCL and a hollow fiber gas cell. In: Druy MA, Crocombe RA, Barnett SM, Profeta LT, editors. Proceedings of SPIE - the international society for optical engineering, 10210; 2017. p. 1021003. doi:10.1117/12.2262612.
[21] Hartmann JM, Boulet C, Robert D. Collisional effects on molecular spectra. Elsevier; 2008. doi:10.1016/B978-0-444-52017-3.X0001-5.
[22] Pieroni D, Nguyen-Van-Thanh, Brodbeck C, Claveau C, Valentin A, Hartmann JM, Gabard T, Champion JP, Bermejo D, Domenech JL. Experimental and theoretical study of line mixing in methane spectra. I. The N_2-broadened $\nu 3$ band at room temperature. J Chem Phys 1999;110(16):7717–32. doi:10.1063/1.478724.
[23] Tran H, Flaud PM, Fouchet T, Gabard T, Hartmann JM. Model, software and database for line-mixing effects in the $\nu 3$ and $\nu 4$ bands of CH_4 and tests using laboratory and planetary measurements-II: H2(and He) broadening and the atmospheres of Jupiter and Saturn. J Quant Spectrosc Radiat Transfer 2006;101(2):306–24. doi:10.1016/j.jqsrt.2005.11.033.
[24] Lee DD, Bendana FA, Schumaker SA, Spearrin RM. Wavelength modulation spectroscopy near 5 μm for carbon monoxide sensing in a high-pressure kerosene-fueled liquid rocket combustor. Appl Phys B 2018;124(5):77. doi:10.1007/s00340-018-6945-6.
[25] Rieker GB, Jeffries JB, Hanson RK. Measurements of high-pressure CO_2 absorption near 2.0 μm and implications on tunable diode laser sensor design. Appl Phys B Lasers Opt 2009;94(1):51–63. doi:10.1007/s00340-008-3280-3.
[26] Bergman TH, Lavine AS, Incropera FP, Dewitt DP. Fundamentals of mass and heat transfer. 7th ed. John Wiley & Sons, Inc.; 2011.
[27] Moin P. Fundamentals of engineering numerical analysis. 2nd ed. Cambridge University Press; 2010.
[28] Modest MF. Radiative heat transfer. 3rd ed. Academic Press; 2013. doi:10.1016/C2010-0-65874-3.